Inorganic Chemistry

Article

pubs.acs.org/IC

Structural, Spectroscopic, and Computational Characterization of the Azide Adduct of Fe^{III}(2,6-diacetylpyridinebis(semioxamazide)), a Functional Analogue of Iron Superoxide Dismutase

Craig T. Gutman,[†] Ilia A. Guzei, and Thomas C. Brunold*

Department of Chemistry, University of Wisconsin—Madison, Madison, Wisconsin 53706, United States

Supporting Information

ABSTRACT: We have prepared and thoroughly characterized, using X-ray crystallographic, spectroscopic, and computational methods, the diazide adduct of $[Fe^{III}(dapsox)(H_2O)_2]^+$ [dapsox = 2,6-diacetylpyridinebis(semioxamazide)], (**1**), a low-molecular weight, functional analogue of iron superoxide dismutase (FeSOD). The X-ray crystal structure of the dimeric form of **1**, $(Na[Fe^{III}(dapsox)(N_3)_2]\cdot DMF)_2$ (**2**) shows two axially coordinated, symmetry inequivalent azides with differing Fe−N_3 bond lengths and Fe−N−N_2 bond angles. This inequivalence of the azide ligands likely reflects the presence of an interdimer hydrogen bonding interaction between a dapsox NH group and the coordinated nitrogen of one of the two azide ligands. Resonance Raman (rR) data obtained for frozen aqueous solution and solid-state samples of **2** indicate that the azides remain inequivalent in solution, suggesting that one of the azide ligands of **1** engages in an intermolecular hydrogen bonding interaction with a water molecule. Density functional theory (DFT) and time-dependent DFT calculations have been used to study two different computational models of **1**, one using coordinates taken from the X-ray crystal structure of **2**, and the other generated via DFT geometry optimization. An evaluation of these models on the basis of electronic absorption, magnetic circular dichroism, and rR data indicates that the crystal structure based model yields a more accurate electronic structure description of **1**, providing further support for the proposed intermolecular hydrogen bonding of **1** in the solid state and in solution. An analysis of the experimentally validated DFT results for this model reveals that the azides have both σ- and π-bonding interactions with the Fe^{III} center and that more negative charge is located on the Fe-bound, rather than on the terminal, nitrogen atom of each azide. These observations are reminiscent of the results previously reported for the azide adduct of FeSOD and provide clues regarding the origin of the high catalytic activity of Fe-dapsox for superoxide disproportionation.

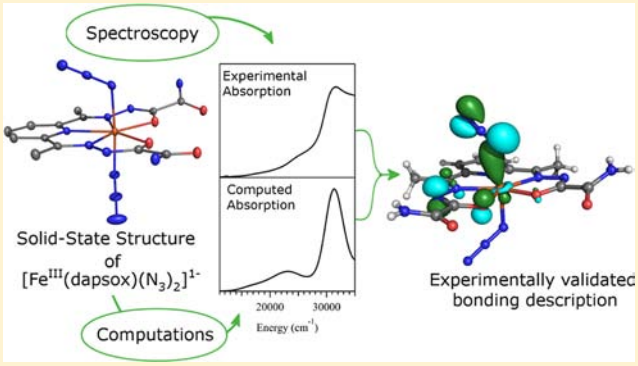

INTRODUCTION

As a result of its ability to generate a wide variety of reactive oxygen and nitrogen species (ROS and RNS), the accumulation of the superoxide radical anion ($O_2^{\bullet-}$) poses a significant threat to aero-tolerant organisms because of the devastating reactions of ROS and RNS with a wide variety of biological macromolecules, including DNA, proteins, and the cellular lipid bilayers.[1,2] To help prevent the formation of ROS and RNS, these organisms produce enzymes called superoxide dismutases (SODs) that catalyze the disproportionation of two equivalents of superoxide and two protons to O_2 and H_2O_2.[1,3,4] While several distinct classes of SODs are known, each differs with respect to their metal cofactor(s) (i.e., Cu/Zn-, Fe-, Mn-, and NiSODs). However, all SODs use ping-pong type mechanisms for $O_2^{\bullet-}$ disproportionation, in which the metal center cycles between two oxidation states (see eqs 1a and 1b).[1,3−7]

$$M(ox)SOD + O_2^{\bullet-} + H^+ \rightarrow M(red)SOD^H + O_2 \quad (1a)$$

$$M(red)SOD^H + O_2^{\bullet-} + H^+ \rightarrow M(ox)SOD + H_2O_2 \quad (1b)$$

Though distinct from the Cu/Zn- and NiSODs, Fe- and Mn-containing SODs are structurally homologous, possessing virtually identical protein folds and active site structures.[6,8−11] In each enzyme, the metal ion resides in a trigonal bipyramidal ligand environment with one aspartate and two histidines in the equatorial plane, and a third histidine residue and a solvent molecule, which is OH^- in the oxidized (M^{III}) state and H_2O in the reduced (M^{II}) state, in the axial positions.[12]

Elevated cellular levels of superoxide have been implicated in a variety of diseases, including several inflammatory disorders, familial amyotrophic lateral sclerosis, Parkinson's disease, and Alzheimer's disease.[13−16] Consequently, there is a significant interest in the discovery and optimization of synthetic, low molecular weight, functional analogues of SOD enzymes. One

Received: May 2, 2013
Published: July 22, 2013

   dx.doi.org/10.1021/ic401098x | Inorg. Chem. 2013, 52, 8909−8918

of the more promising enzyme mimics has been developed by Ivanović-Burmazović and co-workers, based on the so-called dapsox ligand [dapsox = 2,6-diacetylpyridinebis-(semioxamazide)].[17,18] Dapsox is a rigid acyclic dianion that will ligate to a metal in a roughly planar, pentachelate fashion; with the additional ligation of two axial molecules this yields a heptacoordinate, pseudopentagonal bipyramidal metal complex.[18] Previous studies have shown that Fe(dapsox) catalyzes $O_2^{\cdot-}$ disproportionation at a rate approaching that of FeSOD to within about an order of magnitude.[18] On the basis of our combined spectroscopic and computational studies of $[Fe^{III}(dapsox)(H_2O)_2]^+$ (see Figure 1) and $[Fe^{II}(H_2dapsox)(H_2O)_2]^{2+}$, we have recently proposed a two-pronged mechanism in which a combination of a proton uptake coupled to Fe^{III} ion reduction and π-backbonding in the Fe^{II} state are employed by the dapsox ligand to properly tune the $Fe^{III/II}$ redox potential for catalytic activity.[19]

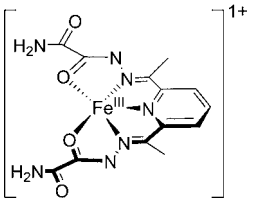

Figure 1. Chemical structure of $[Fe^{III}(dapsox)]^+$.

To probe further the molecular mechanism employed by Fe(dapsox) for superoxide dismutation, it would be desirable to trap and characterize the actual catalytic intermediates. Unfortunately, the high turnover rate ($k_{cat} \sim 10^7$ M^{-1} s^{-1})[18] prevents the trapping of such species. However, it is possible to employ the same approach used in the study of the SOD enzymes, which is to probe the enzyme's interactions with an appropriate substrate analogue. In the case of SOD, the azide (N_3^-) ion is a commonly used analogue, as it possesses the same charge and similar frontier orbitals as $O_2^{\cdot-}$.[6,9,20−28]

Hence, to gain additional insight into the mechanism of catalytic superoxide disproportionation by Fe(dapsox), we have prepared the azide adduct of $[Fe^{III}(dapsox)(H_2O)_2]^+$, and examined the geometric structure of its solid-state dimer, $(Na[Fe^{III}(dapsox)(N_3)_2]\cdot DMF)_2$ (**2**) using X-ray crystallography. The electronic structure of the anionic complex, $[Fe^{III}(dapsox)(N_3)_2]^-$ (**1**), was probed with electronic absorption (Abs), magnetic circular dichroism (MCD), and resonance Raman (rR) spectroscopies. Additionally, we carried out density functional theory (DFT) and time-dependent DFT (TD-DFT) calculations to generate an experimentally validated bonding description for **1**. The results obtained in these studies provide detailed insight into the substrate analogue/Fe^{III}(dapsox) interactions and reveal some interesting similarities between **1** and the azide adduct of Fe^{III}SOD (N_3−Fe^{III}SOD).[27,29]

EXPERIMENTAL SECTION

Synthesis and Materials. Oxamic hydrazide was obtained from TCI America (Portland, OR), while all other reagents including 1−^{15}N isotopically labeled sodium azide (98%) were obtained from Sigma-Aldrich (St. Louis, MO). All reagents were used as received unless otherwise noted. Electrospray ionization mass spectrometry (ESI-MS) data were obtained using a Waters (Micromass) LCT spectrometer equipped with a time-of-flight analyzer. IR spectra were taken on a Bruker TENSOR 27 using ATR techniques.

$[Fe^{III}(dapsox)(H_2O)_2]NO_3$. $[Fe^{III}(dapsox)(H_2O)_2]NO_3$ was synthesized as previously reported[19] with the exception that the product was not purified by recrystallization prior to the reaction with NaN_3.

$[Fe^{III}(dapsox)(N_3)_2]^-$ (1). A 550 mg portion (1.13 mmol) of $[Fe^{III}(dapsox)(H_2O)_2]NO_3$ was dissolved in 10 mL of dimethylformamide (DMF), and 735 mg (11.3 mmol) of NaN_3 was added to yield a dark red solution. The solution was then filtered, and the product isolated by addition of Et_2O until a dark red microcrystalline material was formed. Yield: 421 mg (79%). ESI-MS: m/z = 441 [M − $(N_3)_2$ +MeO +Na]$^+$. IR (ATR, cm^{-1}): 3443 (w), 3330 (w), 2051 [vs (N_3)], 1698 (vs), 1615 (m), 1589 (w), 1564 (s), 1551 (s), 1518 (m), 1371 (w), 1296 (s), 1206 [w (N_3)], 1150 (w), 1023 (w), 813 (w). Red block crystals suitable for crystallographic analysis were obtained by four rounds of crystallization by vapor diffusion of Et_2O into a concentrated DMF solution of **1**.

X-ray Crystallography. *X-ray Crystal Structure Data.* X-ray crystallographic data for $(Na[Fe^{III}(dapsox)(N_3)_2]\cdot DMF)_2$ (**2**) were collected at 100 K using a Bruker SMART APEXII diffractometer with Cu K_α (λ = 1.54178 Å) radiation. The full sphere data collection routine was employed to survey the reciprocal space to the extent of a full sphere to a resolution of 0.82 Å. A total of 21682 data points were harvested by collecting 22 sets of frames with 0.7° scans in ω with an exposure time of 3, 5, or 10 s per frame. These highly redundant data sets were corrected for Lorentz and polarization effects. The absorption correction was based on fitting a function to the empirical transmission surface as sampled by multiple equivalent measurements.[30] A successful solution by direct methods provided most non-hydrogen atoms from the E-map. The remaining non-hydrogen atoms were located in an alternating series of least-squares cycles and difference Fourier maps. Standard uncertainties of the bond distances and angles were computed from the variance-covariance matrix obtained for the structure refined to convergence with the least-squares method. All non-hydrogen atoms were refined with anisotropic displacement coefficients. All hydrogen atoms were included in the structure factor calculation at idealized positions and were allowed to ride on the neighboring atoms with relative isotropic displacement coefficients. Relevant crystallographic data are summarized in Table 1 and selected bond distances and angles are listed in Table 2. Complete crystallographic information is provided as Supporting Information in CIF format.

Spectroscopy. *Electronic Absorption (Abs) and Magnetic Circular Dichroism (MCD) Data.* Room temperature Abs spectra were collected using a Varian Cary 5e spectrophotometer while low temperature Abs and MCD spectra were obtained with a JASCO J-715 spectropolarimeter in conjunction with an Oxford Instruments SM-4000 8 T superconducting magnetocryostat. Circular dichroism and glass-strain contributions to the MCD spectra were removed by subtracting the −7 T data from the +7 T data. All data were collected from either solution samples dissolved in 20:80 (v/v) 100 mM phosphate buffer, pH 2:glycerol or from solid-state mulls prepared by grinding solid **2** and adding polydimethylsiloxane.

Resonance Raman (rR) Data. Samples for rR spectroscopy were prepared as either an ∼18 mM solution of **1** in 100 mM phosphate buffer, pH 2, or as a powdered solid by grinding a sample of **2** with an excess of KBr, and were immediately frozen in liquid N_2. rR data were obtained at 77 K upon excitation with an Ar^+ ion laser (Coherent I-90) with ∼40−60 mW of laser power at the sample, using a ∼135° backscattering arrangement. The scattered light was dispersed with an Acton Research triple monochromator (equipped with 300, 1200, and 2400 grooves/mm gratings) and analyzed with a Princeton Instruments Spec X: 100BR deep-depletion, back-thinned CCD detector.

Computations. *Geometry Optimizations.* The ORCA 2.9.1 software package developed by Dr. Frank Neese[31] was used to perform spin-unrestricted density functional theory (DFT) single-point calculations and geometry optimizations for **1** starting from coordinates taken from the X-ray crystal structure of **2**. On the basis of the spectroscopic data obtained in this work, **1** was described as a high-spin (S = 5/2), Fe^{III} complex. The calculations were performed with Becke's three-parameter hybrid functional for exchange[32,33] and the Lee−Yang−Parr functional for correlation (B3LYP)[34] and an

dx.doi.org/10.1021/ic401098x | Inorg. Chem. 2013, 52, 8909−8918

Table 1. X-ray Crystallographic Data for $(Na[Fe^{III}(dapsox)(N_3)_2]\cdot DMF)_2$ (2)

	$(Na[Fe^{III}(dapsox)(N_3)_2]\ DMF)_2$
empirical formula	$C_{32}H_{40}Fe_2N_{28}Na_2O_{10}$
formula weight	1134.6
temperature	100(1) K
wavelength	1.54178 Å
crystal system	triclinic
space group	$P\bar{1}$
unit cell dimensions	a = 9.6720(9) Å, α = 101.746(8)°
	b = 10.2084(9) Å, β = 90.285(6)°
	c = 11.7514(10) Å, γ = 91.305(6)°
volume	1135.64(17) Å^3
Z	1
d_{calcd}	1.659 Mg/m^3
abs. coeff	6.082 mm^{-1}
$F(000)$	582
θ range	3.84 to 72.26°
reflections collected	21682
independent reflections	4252 [R(int) = 0.0250]
resolution	0.83 Å
goodness-of-fit (F^2)	1.011
final R indices [$I > 2\sigma(I)$]	R1 = 0.0251,
	wR2 = 0.0679
R indices (all data)	R1 = 0.0256,
	wR2 = 0.0683
diff. peak and hole	0.551 and −0.373 e$^-$ Å^{-3}

Table 2. Selected Bond Lengths (Å) and Angles (deg) from the X-ray Crystal Structure of 2

	Bond Lengths		
Fe−O1	2.1092(10)	Fe−O3	2.0521(10)
Fe−N3	2.1648(12)	Fe−N11	2.0531(13)
Fe−N4	2.1776(12)	Fe−N8	2.0990(13)
Fe−N5	2.1828(12)		
	Bond Angles		
O1−Fe−N3	71.82(4)	N8−Fe−O1	91.92(5)
N3−Fe−N4	70.76(5)	N8−Fe−N3	86.66(5)
N4−Fe−N5	71.13(5)	N8−Fe−N4	88.87(5)
N5−Fe−O3	71.93(4)	N8−Fe−N5	90.07(5)
O3−Fe−O1	74.55(4)	N8−Fe−O3	88.98(5)
N11−Fe−O1	90.59(5)	N11−Fe−N8	175.84(5)
N11−Fe−N3	90.97(5)	Fe−N11−N12	121.08(11)
N11−Fe−N4	87.11(5)	Fe−N8−N9	119.02(10)
N11−Fe−N5	89.68(5)	N11−N12−N13	178.10(17)
N11−Fe−O3	94.89(5)	N8−N9−N10	179.68(17)

integration grid of size 4 (302 Lebedev points). The polarized split-valence SV(P) basis set[35] and the SV/C auxiliary basis set[36] were used for all atoms except for the Fe ion and the ligating nitrogen and oxygen atoms, for which Ahlrich's polarized-triple-ζ-valence (TZVP) basis set[37] with one polarization function was employed. The geometry-optimized coordinates for the two computational models of **1** described in the text are provided in the Supporting Information, Tables S1 and S3.

Time Dependent DFT (TD-DFT). TD-DFT calculations within the Tamm-Dancoff approximation[38,39] were also performed with the ORCA 2.9.1 software package[31] on both the geometry-optimized and the X-ray crystal structure based models of **1** using the same basis sets and functionals as for the single-point and geometry-optimization calculations. A total of 50 excited states were constructed from all MOs within ±3 hartree of the highest occupied molecular orbital (HOMO)/lowest unoccupied molecular orbital (LUMO) energy gap. The TD-DFT results were used to simulate Abs spectra assuming that each electronic transition gives rise to a Gaussian band with a full width at half-maximum of 3330 cm^{-1}, a value that was chosen on the basis of our spectral analysis of the experimental data. Isosurface plots of the molecular orbitals (MOs) and electron density difference maps (EDDMs) were generated using the PyMol program with isodensity values of 0.05 au and 0.003 au, respectively.[40]

Frequency Calculations. Vibrational frequencies as well as the IR and normal Raman intensities were calculated with the Gaussian '09 software package[41] using the same geometries, basis sets, and functionals as for the TD-DFT calculation. These results were used to construct Raman spectra by assuming that each vibrational transition gives rise to a Gaussian band with a full width at half-maximum of 13 cm^{-1}.

RESULTS

Experimental Studies. *Crystal Structure.* The 0.83 Å resolution X-ray crystal structure of $(Na[Fe^{III}(dapsox)(N_3)_2]\cdot DMF)_2$ (**2**) reveals a dimer of pentagonal bipyramidal complexes, where in each the dapsox ligand coordinates equatorially in a pentachelate fashion and two azide ions coordinate axially (Figure 2). The unit cell also contains a Na^+ counterion located between the two "arms" of the dapsox ligand, where it forms favorable polar contacts with the four carbonyl oxygens, and a DMF solvent molecule disordered over two positions, with the major component present 81.4(3)% of the time. The two $[Fe^{III}(dapsox)(N_3)_2]^-$ (**1**) units have identical geometries as a result of the dimer occupying a crystallographic inversion center. The dapsox ligand adopts a fairly planar configuration around the Fe^{III} center with the five ligating atoms having a mean deviation from planarity of 0.054 Å and the central Fe^{III} ion being 0.0251(6) Å displaced from this plane. Additionally, the sum of the four chelate angles and the O1−Fe1−O3 angle (Table 2) for the dapsox ligand is 369.19°, close to the ideal value of 360° for a planar structure.

The two azides complete the pseudopentagonal bipyramidal geometry around the central iron ion with a close to linear N8−Fe1−N11 bond angle of 175.84(5)° and a N9−N8−N11−N12 torsion angle of 73.529(6)°. They are symmetry inequivalent and bind to the iron center in a bent manner with Fe−N−N_2 bond angles of 119.02(10)° and 121.08(11)°. Further highlighting the inequivalence of these azides are the Fe−N_3 bond lengths of 2.0531(13) Å and 2.0990(13) Å. The distinct nature of the two azide ligands likely reflects the presence of an interdimer H-bonding interaction between the H(N7) atom of one molecule of **2** and the N8 (azide) of an adjacent molecule of **2** (the H(N7) ··· N8 and N7 ··· N8 distances in the crystal structure are 2.300 and 3.151 Å, respectively). This hydrogen bonding interaction would be expected to weaken, and thus lengthen, the Fe−N8 bond relative to the Fe−N11 bond, which is indeed observed experimentally (bond distances of 2.099 and 2.053 Å, respectively).

Abs and MCD Spectra. The room temperature (RT) Abs spectrum of **1** (Figure 3, top) exhibits a prominent band centered at 31 500 cm^{-1} ($\varepsilon \approx 20\,000$ M^{-1} cm^{-1}) and a more intense feature peaking at >40 000 cm^{-1} ($\varepsilon \geq 25\,000$ M^{-1} cm^{-1}) as well as two shoulders located at 25 000 cm^{-1} ($\varepsilon \approx 5000$ M^{-1} cm^{-1}) and 34 700 cm^{-1} ($\varepsilon \approx 18\,800$ M^{-1} cm^{-1}). In the corresponding 4.5 K, frozen solution MCD spectrum (Figure 3, bottom), four broad bands with alternating signs are observed at ∼17 300, 24 500, 31 600, and 37 200 cm^{-1}. The intensities of these bands are temperature dependent (Supporting Information, Figure S1), indicating that the corresponding transitions gain MCD intensity via a C-term

dx.doi.org/10.1021/ic401098x | Inorg. Chem. 2013, 52, 8909−8918

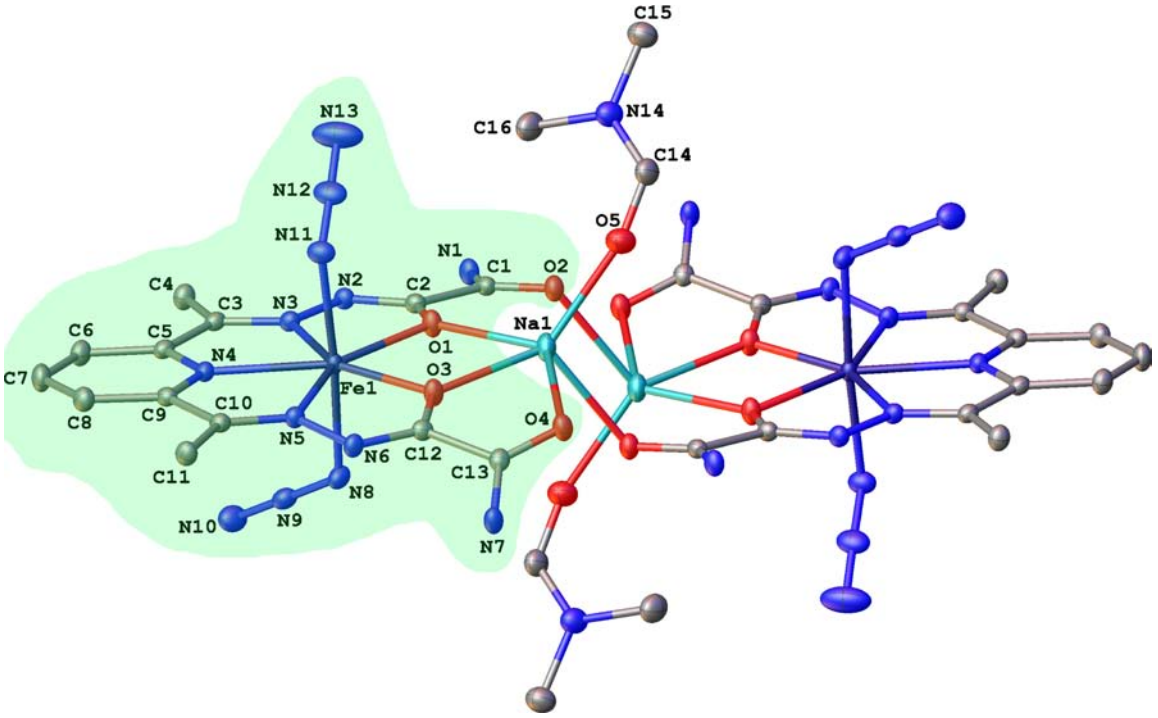

Figure 2. Thermal ellipsoid representation (50% probability boundaries) of the X-ray crystal structure of **2**. All hydrogen atoms and the minor components of the disordered DMF molecule are omitted for clarity. One of the two equivalent $[Fe^{III}(dapsox)(N_3)_2]^-$ (**1**) units is highlighted in green.

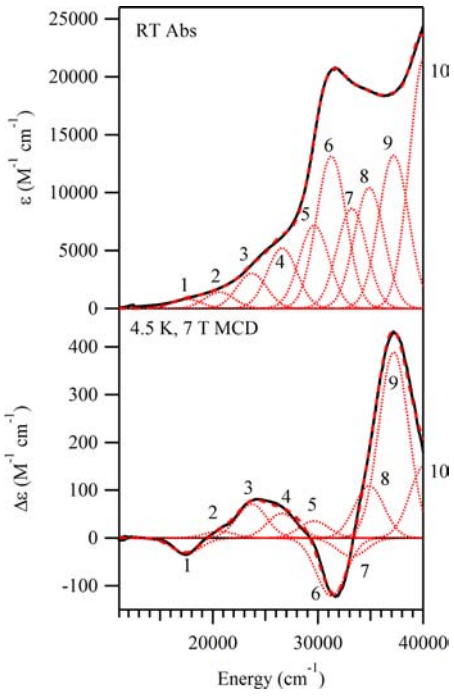

Figure 3. RT Abs (top) and 4.5 K 7 T MCD (bottom) solution spectra of **1** (thick black lines). Individual Gaussian bands are shown as thin dotted red lines, and the simulated spectra are shown as thick dashed red lines.

mechanism, as expected for a paramagnetic species like **1**. To resolve the individual transitions contributing to the Abs and MCD spectra, these data were iteratively fit with the minimum acceptable number of Gaussian bands of constant width. Good agreement between the experimental and simulated spectra over the entire 11 000−40 000 cm^{-1} range was achieved with 10 Gaussian bands (Figure 3 and Table 3). The low C/D ratios[42] associated with the features observed in the Abs and MCD spectra indicate that the corresponding transitions have primarily ligand-to-metal charge transfer (LMCT) character. Specific spectral assignments are provided below.

Table 3. Spectral Parameters from the Iterative Fits of the Abs and MCD Data of 1

band	E (cm^{-1})	ε (M^{-1} cm^{-1})	Δe (M^{-1} cm^{-1})	C/D ratio[a]
1	17515	814	−31.7	0.037
2	20639	1401	14.0	0.010
3	23713	3033	71.0	0.022
4	26599	5216	51.6	0.009
5	29643	7178	35.4	0.004
6	31276	13132	−121.2	0.009
7	33224	8626	−38.5	0.004
8	34872	10425	109.0	0.010
9	37200	13207	388.3	0.028
10	40123	21716	150.4	0.007

[a] $C/D = (kT/\beta H)(\Delta\varepsilon/\varepsilon) = 0.9576(\Delta\varepsilon/\varepsilon)$ when H = 7.0 T and T = 4.5 K.

rR Spectroscopy. On the basis of our previous study of N_3−Fe^{III}SOD,[27] a single azide that is terminally bound to an iron atom will give rise to three characteristic rR features. These features are the Fe−N_{azide} stretch (ν(Fe−N_3)) located around 370 cm^{-1}, the symmetric intra-azide stretch ($\nu_s(N_3^-)$) at ∼1350 cm^{-1}, and the asymmetric intra-azide stretch ($\nu_{as}(N_3^-)$) near 2050 cm^{-1}. Alternatively, a detailed characterization of a synthetic Fe^{III} complex possessing two symmetry inequivalent, *cis*-bound azides revealed two pairs of azide related rR features centered ∼375 and 2060 cm^{-1}.[43] These features were assigned

dx.doi.org/10.1021/ic401098x | Inorg. Chem. 2013, 52, 8909−8918

as the ν(Fe−N_3) and $\nu_{as}(N_3^-)$ modes associated with the two azides. Notably, no features associated with the $\nu_s(N_3^-)$ mode were observed.

In the frozen-solution rR spectrum of **1** obtained with 20 490 cm^{-1} (488 nm) laser excitation, four features are observed that are sensitive to 1-^{15}N isotopic substitution of the coordinated azide ligands (Figure 4 and Table 5). The feature centered at

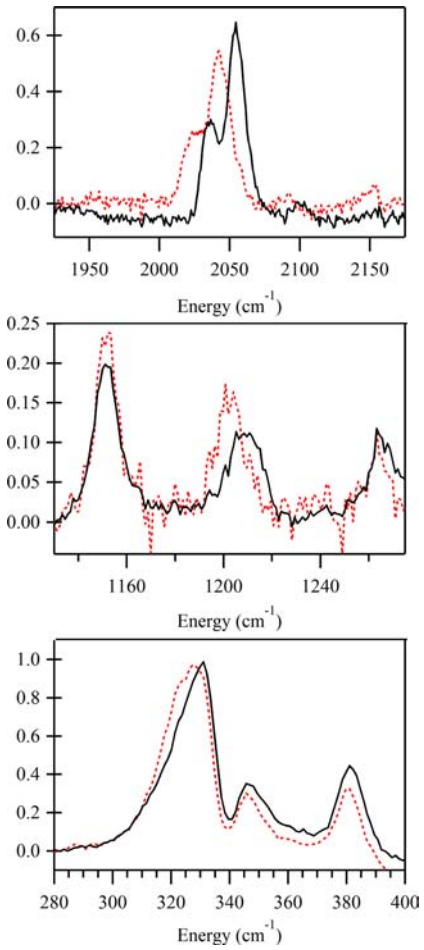

Figure 4. Frozen-solution rR spectra of **1** at 77 K obtained with 20 490 cm^{-1} (488 nm) laser excitation. Spectra of **1** synthesized with natural abundance azide are shown in black while spectra of **1** prepared with ^{15}N terminally labeled azide are shown as dashed, red lines. Selected regions are shown to highlight the four isotopically sensitive features arising from the $\nu_{as}(N_3^-)$ stretches (top), the $\nu_s(N_3^-)$ stretch (middle), and the ν(Fe−N_3) stretch (bottom). For ease of comparison the spectra have been normalized using the ν(Fe−N_3) peak.

331 cm^{-1} is attributed to the ν(Fe−N_3) mode involving the coupled motion of the two azides, while the feature centered at 1210 cm^{-1} is attributed to the in-phase $\nu_s(N_3^-)$ motion of the azides ligands. The remaining features at 2035 and 2055 cm^{-1} are assigned to the individual $\nu_{as}(N_3^-)$ stretches of the two azide ligands. Examination of the rR spectrum of a solid-state sample of **2** obtained under the same conditions shows four analogous features (Supporting Information, Figure S5), indicating that the geometry of this complex in the solid state is preserved in solution. Additionally, rR spectra obtained with both lower and higher laser excitation energies (19 460 and 21 830 cm^{-1}, respectively) show that the intensity ratio for the pair of features near 2050 cm^{-1} remains constant as a function of excitation energy (Supporting Information, Figures S3 and S4).

It can thus be concluded that these features arise from independent $\nu_{as}(N_3^-)$ stretches associated with two distinct azide ligands rather than from in-phase and out-of-phase combinations of the coupled vibrations, as in the latter scenario the in-phase combination would be preferentially resonance enhanced[44] and as such the intensity ratio of the 2035/2055 cm^{-1} features would change as a function of excitation energy used in the rR experiment.

Computational Studies. *Computational Models.* To assign the observed Abs and MCD features and to obtain a quantitative bonding description for **1**, electronic structure calculations were performed using two different models. The first model ($\mathbf{1}_{xtal}$) was constructed using the coordinates for one of the $[Fe^{III}(dapsox)(N_3)_2]^-$ units from the X-ray crystal structure of **2**, while the second ($\mathbf{1}_{opt}$) was obtained by a DFT geometry optimization of $\mathbf{1}_{xtal}$. As seen in Table 4, the

Table 4. Selected Geometric Parameters for the Different Computational Models of 1

	X-ray crystal structure $\mathbf{1}_{xtal}$	DFT optimized $\mathbf{1}_{opt}$	DFT optimized $\mathbf{1}_{opt}\cdot\mathbf{H_2O}$
	Bond Lengths (Å)		
Fe−O1	2.109	2.121	2.149
Fe−N3	2.165	2.290	2.256
Fe−N4	2.178	2.305	2.295
Fe−N5	2.183	2.262	2.285
Fe−O3	2.052	2.151	2.101
Fe−N11	2.053	2.042	2.031
Fe−N8	2.099	2.041	2.075
	Bond Angles (deg)		
O1−Fe−N3	71.8	70.5	70.6
N3−Fe−N4	70.8	68.6	68.8
N4−Fe−N5	71.1	68.6	68.7
N5−Fe−O3	71.9	70.6	70.5
O3−Fe−O1	74.6	81.8	81.2
N11−Fe−N8	175.8	170.2	171.6
Fe−N11−N12	121.1	129.4	129.9
Fe−N8−N9	119.0	129.4	126.4
	Torsion Angles (deg)		
N9−N8−N11−N12	73.61	1.88	2.70

geometry-optimized model differs from the crystallographically determined structure in two important ways: (i) the Fe−N/O(dapsox) bond lengths are significantly elongated (by up to 0.13 Å) compared to those in the crystal structure and (ii) the two axial azides have become symmetry equivalent with identical Fe−N_3 bond lengths (2.04 Å) and Fe−N−N_2 bond angles (129.4°). Because of these differences, the computed ground-state and excited-state properties of both models will be presented below.

Calculated MO Diagrams. Spin-unrestricted single point DFT calculations were carried out to compute the MO energies and compositions of $\mathbf{1}_{xtal}$ and $\mathbf{1}_{opt}$. Because of their reduced exchange-stabilization, the unoccupied Fe 3d-based spin-down MOs are higher in energy than their occupied spin-up counterparts[45] and, consequently, less strongly mixed with the ligand frontier orbitals. Therefore, for ease of analysis, only the spin-down MOs will be discussed here.

The splitting pattern of the unoccupied Fe 3d-based spin-down MOs of either model is as expected for a complex with approximate D_{5h} symmetry (Figure 5). Lowest in energy are the Fe $3d_{yz}$ (118b) and $3d_{xz}$ (120b and 119b in $\mathbf{1}_{xtal}$ and $\mathbf{1}_{opt}$,

dx.doi.org/10.1021/ic401098x | Inorg. Chem. 2013, 52, 8909−8918

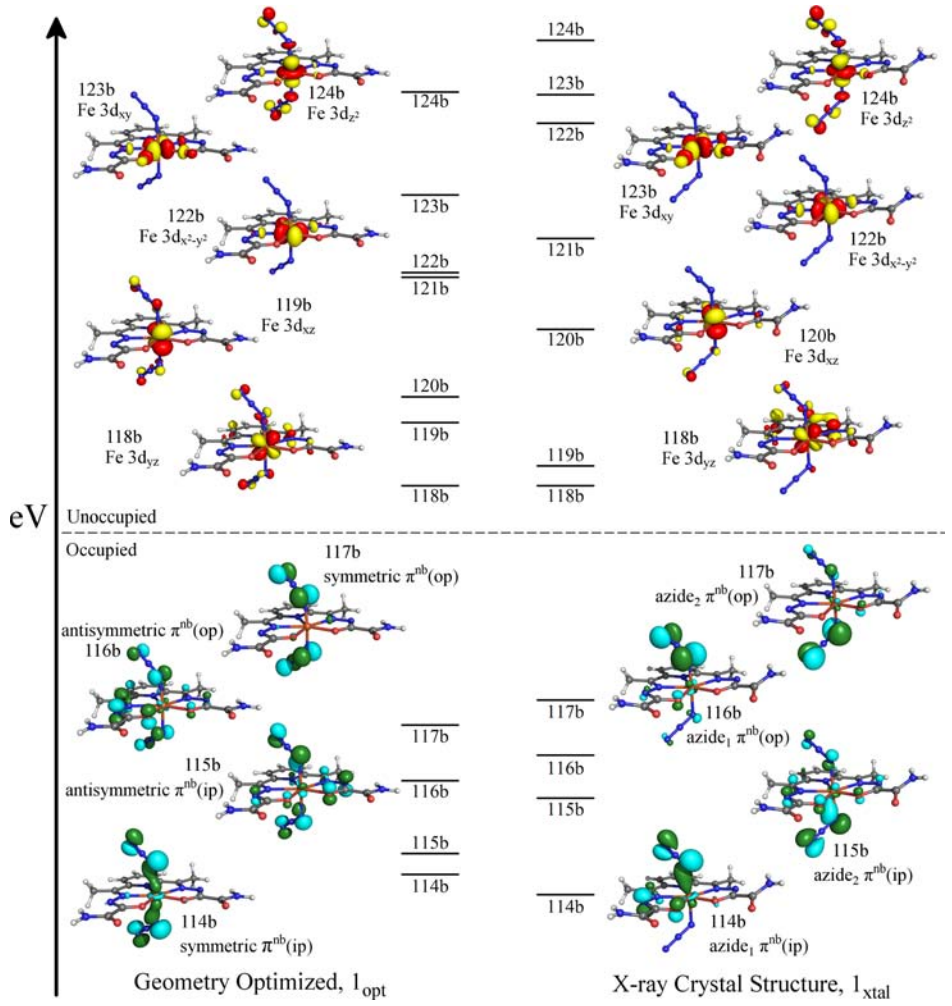

Figure 5. Energy-level diagrams of the frontier spin-down MOs, as obtained from spin-unrestricted DFT calculations on the geometry-optimized ($\mathbf{1}_{opt}$, left) and the crystal structure derived ($\mathbf{1}_{xtal}$, right) models of **1**. For ease of comparison the energies of all MOs have been shifted so as to align the LUMOs. Isosurface plots of the unoccupied Fe 3d-based MOs and the occupied azide based MOs are shown to the sides.

respectively) based MOs, followed by the Fe $3d_{x^2-y^2}$ (122b) and $3d_{xy}$ (123b) based MOs and, highest in energy, the Fe $3d_{z^2}$ based MO (124b). Notably, the splitting of the Fe 3d-based spin-down MOs is significantly smaller in $\mathbf{1}_{opt}$ than in $\mathbf{1}_{xtal}$. This difference reflects the weaker Fe−dapsox antibonding interactions in $\mathbf{1}_{opt}$ as a result of the significantly larger average Fe−N/O(dapsox) bond length in this model.

As expected from the different orientations of the axial ligands in $\mathbf{1}_{xtal}$ and $\mathbf{1}_{opt}$, the azide based MOs vary significantly between the two computational models studied. Each azide ligand has two π^{nb} orbitals, one of which is oriented in-plane (ip) and the other out-of-plane (op) with respect to the Fe−N_3 plane. In $\mathbf{1}_{xtal}$, the two azides are geometrically inequivalent and, as such, the calculated MO diagram (Figure 5) shows two sets of azide based, Fe−N_3 σ- and π-bonding MOs (MOs 114b/116b and MOs 115b/117b for the upper and lower azides, respectively). Alternatively, in $\mathbf{1}_{opt}$ the azides have reoriented so as to become geometrically equivalent. Thus, both azide ligands now contribute equally to the frontier MOs; that is, the π^{nb}(ip) and π^{nb}(op) orbitals on the two azides are coupled either symmetrically or antisymmetrically with respect to reflection about the equatorial pseudo-mirror plane. This results in four frontier MOs of $\mathbf{1}_{opt}$ having significant azide character: the strongly Fe−N_3 σ-bonding and symmetric π^{nb}(ip) based MO 114b, the weakly Fe−N_3 π-bonding and antisymmetric π^{nb}(ip) based MO 115b, the strongly Fe−N_3 π-bonding and antisymmetric π^{nb}(op) based MO 116b, and the nonbonding, symmetric π^{nb}(op) based MO 117b (Figure 5).

Calculated Electronic Absorption Spectra. To calculate the electronic transition energies and Abs intensities for $\mathbf{1}_{xtal}$ and $\mathbf{1}_{opt}$, TD-DFT computations were performed. In each case, the calculated Abs spectrum is in good agreement with the experimental spectrum (Figure 6). The nature of the calculated electronic transitions (e.g., ligand field, LMCT, or $\pi \rightarrow \pi^*$) was determined on the basis of electron density difference maps (EDDMs), which provide visual representations of how the electron density changes between the ground state and the excited states during an electronic transition. The EDDMs for the relevant transitions (identified by Roman numerals I−IV) corresponding to experimental bands 2, 3, 5, and 6, are shown in Figure 7. Examination of these plots reveals that the low energy features in the computed Abs spectra are due to charge transfer (CT) transitions that are primarily $N_3^- \rightarrow Fe^{III}$ in nature. Alternatively, the transitions associated with the higher-energy bands have predominant $dapsox^{2-} \rightarrow Fe^{III}$ CT character. These computational predictions are consistent with the fact that the occupied MOs with significant azide character are

dx.doi.org/10.1021/ic401098x | Inorg. Chem. 2013, 52, 8909−8918

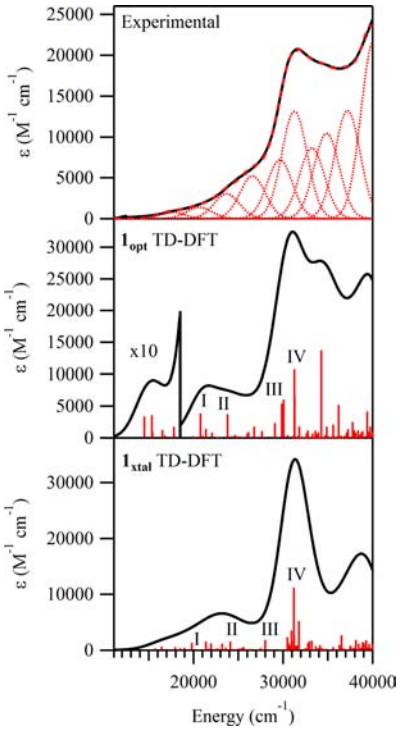

Figure 6. Experimental RT Abs spectrum of **1** (top) and TD-DFT computed Abs spectra for the $\mathbf{1}_{opt}$ and $\mathbf{1}_{xtal}$ models (middle and bottom, respectively). Selected transitions in the computational spectra are labeled with Roman numerals.

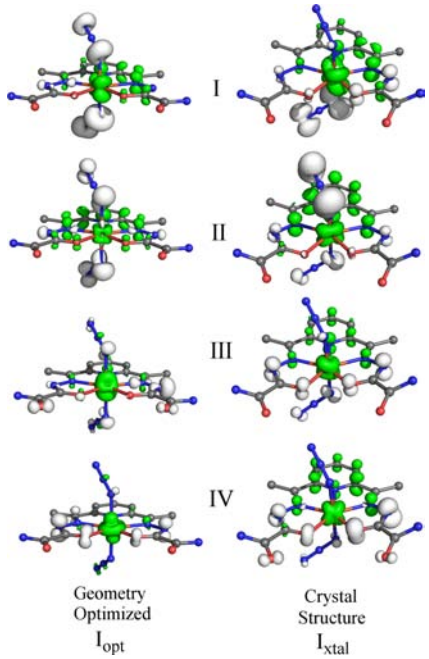

Figure 7. EDDMs for selected TD-DFT calculated electronic transitions of $\mathbf{1}_{opt}$ (left) and $\mathbf{1}_{xtal}$ (right). White and green represent electron density loss and gain, respectively.

higher in energy than those derived from the dapsox ligand (Figure 5).

While the TD-DFT calculated Abs spectra for both models appear quite similar to each other and, as a whole, are in good agreement with the experimental data, a closer examination of the computational results reveals some interesting differences. First, a comparison of the EDDMs for the low-energy transitions I–III (Figure 7) indicates that the compositions of these transitions vary significantly depending on which model is used. As expected from the geometric and electronic equivalencies of the axial ligands in $\mathbf{1}_{opt}$, transitions I–III are predicted to involve near-equal charge transfer from both of the azides to the Fe^{III} center. Alternatively, for $\mathbf{1}_{xtal}$ these transitions have distinct contributions from the azides. Second, by comparing the high-energy region of the computed spectra (above 30 000 cm^{-1}) it is apparent that the results for $\mathbf{1}_{opt}$ are in better agreement with the experimental data. Examination of the EDDMs for both models (Figure 7) reveals that transitions III and IV are mostly $dapsox^{2-} \rightarrow Fe^{III}$ CT in nature. However, in the case of $\mathbf{1}_{xtal}$, they additionally contain a substantial amount of $\pi \rightarrow \pi^*$ character. This finding, combined with the general lack of pure $\pi \rightarrow \pi^*$ excitations at higher energy, indicates that the energy splitting of the $dapsox^{2-}$ π and π^* orbitals is somewhat underestimated in $\mathbf{1}_{xtal}$.

Calculated Raman Spectra. To aid in the interpretation of the experimental rR spectra of **1** and to further evaluate our computational models, additional DFT computations were performed to predict the Raman spectra of $\mathbf{1}_{xtal}$ and $\mathbf{1}_{opt}$. As shown in Figure 8 and Table 5, both models reproduce the experimentally observed frequencies and isotopic shifts upon $^{14}N \rightarrow {}^{15}N$ substitution of the Fe-bound N atoms of the azides quite well for the $\nu(Fe-N_3)$ vibration, but to a lesser degree for the $\nu_s(N_3^-)$ vibration. Because of the different orientations of the azide ligands in $\mathbf{1}_{opt}$ and $\mathbf{1}_{xtal}$, the computed Raman spectra in the region of the $\nu_{as}(N_3^-)$ vibration are significantly different. For $\mathbf{1}_{opt}$, two distinct $\nu_{as}(N_3^-)$ based features are predicted; however, they are separated by only 6 cm^{-1} while the experimental splitting is 20 cm^{-1}. Additionally, the lower energy feature is much less intense than the higher energy one, with an intensity ratio of ~1:5 versus ~1:2 determined experimentally. Finally, because of the symmetry equivalence of the two azides in $\mathbf{1}_{opt}$, the lower and higher energy vibrations correspond to, respectively, the out-of-phase and in-phase combinations of the individual $\nu_{as}(N_3^-)$ stretches of the two azides. Since only the in-phase combination is totally symmetric (as confirmed by the calculated depolarization ratios of 0.75 versus 0.32 for the lower and higher energy vibrations, respectively), the higher energy feature should be strongly enhanced in the rR spectrum over the lower energy one,[44] an effect not observed experimentally (*vide supra*). In comparison with $\mathbf{1}_{opt}$, the results obtained from the Raman calculation for $\mathbf{1}_{xtal}$ agree much better with the experimental data. Again, two $\nu_{as}(N_3^-)$ stretches are calculated; however, the frequency difference of 29 cm^{-1} and intensity ratio of ~1:3 are much closer to the experimental values. Because in $\mathbf{1}_{xtal}$ the azides are symmetry inequivalent, each of the two calculated $\nu_{as}(N_3^-)$ vibrations is associated with only one of the azides. For this reason, along with the fact that the $N_3^- \rightarrow Fe^{III}$ charge transfer transitions for both azides have comparable energies (Figure 6), neither vibration would be preferentially resonance enhanced over the other, and thus, the relative rR intensities of the corresponding features should not vary substantially as a function of excitation energy. This prediction is consistent with the experimental results obtained for **1** (*vide supra*).

Effect of Intermolecular Hydrogen Bonding. As mentioned above, the inequivalence of the two azide ligands in the X-ray crystal structure of **2** likely reflects the presence of an interdimer hydrogen bonding interaction between the H(N7) atom of dapsox of one monomeric complex **1** and the azide

dx.doi.org/10.1021/ic401098x | *Inorg. Chem.* 2013, 52, 8909–8918

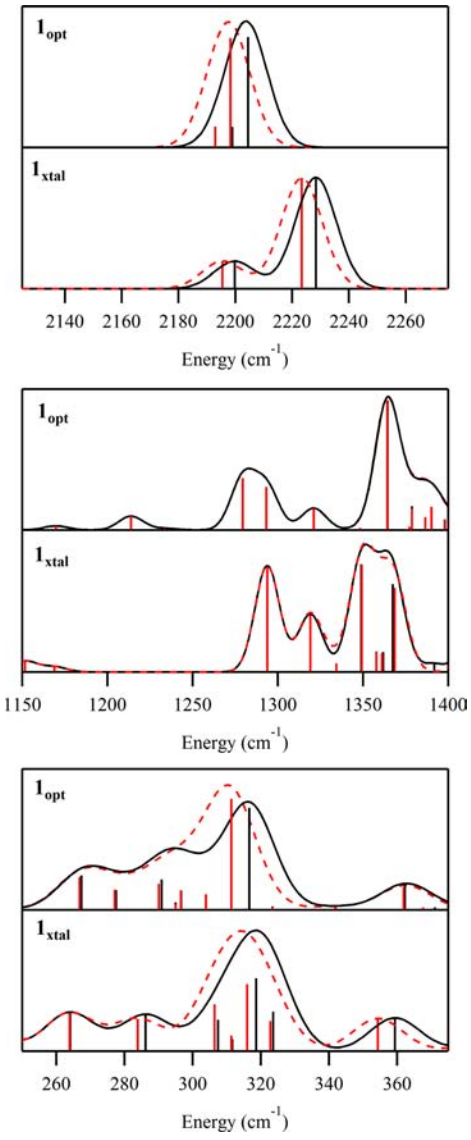

Figure 8. Selected regions of the DFT calculated Raman spectra for models $\mathbf{1}_{opt}$ and $\mathbf{1}_{xtal}$ (upper and lower, respectively). $Fe(N_3)$ spectra are shown in black and the $Fe(^{15}NN_2)$ spectra are shown as red, dashed lines. The vertical sticks (black and red for $Fe(N_3)$ and $Fe(^{15}NN_2)$, respectively) depict the energies and intensities of individual vibrations.

nitrogen N8 of another monomer. On the basis of our analysis of the MCD and rR spectra of **2** within the framework of DFT calculations, we conclude that this inequivalence persists in frozen-solution samples. To evaluate the possibility that in aqueous solution N8 accepts a hydrogen bond from a water molecule, we performed an additional DFT geometry optimization for a model of **1** containing an outer-sphere water molecule ($\mathbf{1}_{opt}\cdot\mathbf{H_2O}$) that was originally placed at an N8···H(OH) distance of 2.30 Å (corresponding to the H(N7)···N8 distance in the X-ray crystal structure of **2**). During the geometry optimization, the N8···H(OH) distance decreased to 2.02 Å, signifying a relatively strong hydrogen bonding interaction. Importantly, as summarized in Table 4, the presence of this hydrogen bond in the optimized $\mathbf{1}_{opt}\cdot\mathbf{H_2O}$ model causes the two azide ligands to become inequivalent, with Fe−N_3 bond lengths of 2.031 and 2.075 Å (vs 2.053 and 2.099 Å in $\mathbf{1}_{xtal}$) and Fe−N−N_2 bond angles of 129.9° and 126.4° (vs 121.1° and 119.0° in $\mathbf{1}_{xtal}$). Thus, the differences in Fe−N_3 bond lengths and Fe−N−N_2 bond angles observed experimentally for **1** are well reproduced in $\mathbf{1}_{opt}\cdot\mathbf{H_2O}$, lending strong support to the hypothesis that an intermolecular hydrogen bonding interaction is largely responsible for the inequivalence of the azide ligands in the solid-state structure and aqueous solutions of **2**.

DISCUSSION

As elevated cellular levels of superoxide have been implicated in a variety of diseases,[13−16] the development and optimization of functional SOD mimics has recently attracted significant research interest. To improve the existing SOD mimics, it would be desirable to have a detailed knowledge of their catalytic mechanisms. However, the most promising mimics react so rapidly with O_2^- that the reaction intermediates are too short-lived to be trapped and characterized. As a resort, it is useful to study the interaction of SOD mimics with substrate analogues, such as the azide ion.

In this study we have determined the first X-ray crystal structure of the azide adduct of one promising small molecule functional mimic of FeSOD, $(Na[Fe^{III}(dapsox)(N_3)_2]\cdot DMF)_2$ (**2**). The structure of **2** reveals that upon addition of NaN_3 to a solution of $[Fe^{III}(dapsox)(H_2O)_2]^+$, both of the axial solvent ligands are replaced by azide ions, while the dapsox ligand remains coordinated in a planar, pentachelate fashion. The presence of a single sodium ion per monomeric complex **1** indicates that the dapsox ligand is doubly deprotonated, as in the case of $[Fe^{III}(dapsox)(H_2O)_2]^+$.[18,46] Interestingly, the two

Table 5. Vibrational Frequencies (cm^{-1}) for the Relevant Normal Modes Associated with the Azide Ligands as Obtained Experimentally for 1 and from DFT Computations using the Geometry-Optimized ($\mathbf{1}_{opt}$) and Crystal Structure Based ($\mathbf{1}_{xtal}$) Models

				DFT-computed					
	experimental (**1**)			$\mathbf{1}_{opt}$			$\mathbf{1}_{xtal}$		
normal mode	$Fe(N_3)_2$	$Fe(^{15}NN_2)_2$	$\Delta\nu$	$Fe(N_3)_2$	$Fe(^{15}NN_2)_2$	$\Delta\nu$	$Fe(N_3)_2$	$Fe(^{15}NN_2)_2$	$\Delta\nu$
ν (Fe−N_3^-)	331	327	4	371	368	3	359	354	5
				387	386	1			
ν_s (N_3^-)	1210	1202	8	1404	1392	12	1353	1334	19
				1405	1396	9	1362	1359	3
							1368	1361	7
							1392	1370	22
ν_{as} (N_3^-)	2035	2023	12	2199	2193	6	2200	2196	4
	2055	2043	12	2205	2199	6	2229	2224	5

dx.doi.org/10.1021/ic401098x | Inorg. Chem. 2013, 52, 8909−8918

axial azides of **1** are inequivalent, with differing Fe−N−N_2 bond angles and Fe−N_3 bond lengths. Presumably, this inequivalence reflects the presences of an interdimer hydrogen bonding interaction involving one of the coordinated azide nitrogens, as described in the Results section.

Evaluation of Our Computational Models. In the course of our studies of **1**, two different computational models were considered; namely, the geometry-optimized $\mathbf{1}_{opt}$ and the crystal structure based $\mathbf{1}_{xtal}$. These models differ in two significant ways: (i) $\mathbf{1}_{opt}$ features weaker Fe−N/O(dapsox) bonding interactions, as indicated by the increased bond lengths, and (ii) the axial azides in $\mathbf{1}_{opt}$ are symmetry equivalent and bound in a more linear fashion, with increased Fe−N−N_2 bond angles of 129° vs 119° and 121° in $\mathbf{1}_{xtal}$. An examination of the TD-DFT predicted Abs spectra reveals that both models accurately reproduce the energies and intensities of the $N_3^- \rightarrow Fe^{III}$ and $dapsox^{2-} \rightarrow Fe^{III}$ CT transitions, though the energies of the $dapsox^{2-}$ $\pi \rightarrow \pi^*$ transitions are somewhat underestimated with the $\mathbf{1}_{xtal}$ model. However, the calculated Raman spectrum for $\mathbf{1}_{xtal}$ is in much better agreement with the experimental results than that obtained with $\mathbf{1}_{opt}$ (see Results section).

As a major goal of this study was to obtain quantitative insight into the Fe−N_3 bonding interactions in **1**, the best suited computational model to consider is the one that most closely reproduces all of the spectral signatures of the diazide-Fe^{III} unit. While both models successfully predict the energies and intensities of the $N_3^- \rightarrow Fe^{3+}$ CT transitions, only $\mathbf{1}_{xtal}$ adequately reproduces the experimentally observed rR behavior for the $\nu_{as}(N_3)$ vibrations of **1**. The use of the crystal structure based model is further justified by the fact that our experimental MCD and, in particular, rR spectra are relatively unchanged when collected using either frozen solution or solid-state samples (cf. Figure 3 and Supporting Information, Figure S2 for the MCD spectra and Figure 4 and Supporting Information, Figure S5 for the rR spectra). On the basis of these considerations, we propose that the inequivalence of the two azide ligands revealed by the crystal structure of **2** persists in aqueous solution. In support of this proposal, the differences in Fe−N_3 bond lengths and Fe−N−N_2 bond angles observed experimentally are well reproduced in the optimized model $\mathbf{1}_{opt}\cdot\mathbf{H_2O}$, which features an outer-sphere water molecule at an N8···H(OH) distance of 2.02 Å (see Table 4).

Nature of Fe−N_3 Bonding in 1 and Related Species. As the two π^{nb} orbitals on each azide of **1** are oriented either in-plane (ip) or out-of-plane (op) with regards to the Fe−N_3 plane, they engage in distinct bonding interactions with the Fe^{III} ion. Specifically, the π^{nb}(ip) orbitals have significant overlap with the Fe-3d_{z^2} orbital, leading to strong σ-bonding interactions, while the π^{nb}(op) orbitals are able to interact with the Fe-3d based orbitals in a π-bonding fashion. This pattern of both strong σ- and π-bonding, due to the end-on, bent coordination geometry of the azide ligands, is consistent with the Fe^{III}−N_3 bonding description established previously for N_3−Fe^{III}SOD.[27,29] The two Fe−N_3 bonds in **1** are quite similar in terms of both their natures and strengths, which is quite different from what we found in a previous study of another diazide iron(III) complex with an FeSOD-like coordination sphere.[43] In this latter complex, the two azide ligands are located *cis* (as opposed to *trans* in **1**) to each other and thus engage in distinct Fe−N_3 bonding interactions, with differing Fe−N−N bond angles (123.7° and 132.8°) and Fe−N_3 bond lengths (1.98 Å and 2.00 Å). These differences resulted in the energies of the π^{nb} based MOs for each azide to differ by ∼4000 cm^{-1}, causing the appearance of two sets of $N_3^- \rightarrow Fe^{III}$ CT transitions associated with the two distinct azides. As a result, in the rR spectrum of this complex the two features arising from the individual ν(Fe−N_3) stretches of each azide are preferentially resonance enhanced at different laser excitation energies.[43]

Implications for the Mechanism of SOD Catalysis. Consistent with the bonding description established for N_3−Fe^{III}SOD,[27] our DFT results suggest that in **1** the Fe^{III}-bound nitrogen atom of each azide ion carries more negative charge than the terminal nitrogen, as judged on the basis of a Loewdin atomic charge analysis. The computational prediction of larger negative charges on the coordinated versus terminal nitrogen atoms of the azide ligands is corroborated by the experimental observation of an interdimer H(N7)···N8 hydrogen bonding interaction in the crystal structure of **2** (see above). This prediction is also consistent with the composition of the Fe-3d_{z^2} based spin-down MO (see Figure 9). As this orbital is unoccupied, any contributions from the azide π^{nb}(ip) orbitals are due to delocalization of hole character from the Fe^{III} center and reflect the degree of $N_3^- \rightarrow Fe^{III}$ charge transfer within the azide π^{nb}(ip) based, occupied MOs. In the case of the Fe-3d_{z^2} derived spin-down MO, it is the terminal nitrogen of each azide ligand that provides the largest contribution, and thus donates the most charge to the Fe^{III} center. This charge distribution suggests that if superoxide binds in a similar manner as azide, as expected, then (i) a large degree of electronic coupling will exist between O_2^- and Fe^{III}, thereby reducing the Franck−Condon barrier to electron transfer, and (ii) the proximal oxygen will be activated toward protonation over the terminal one. Protonation of the proximal oxygen would yield a significantly weaker Fe−hydroperoxide bond, thereby facilitating product release. The combination of these two factors is likely to play a key role with regards to the rapid reaction between $[Fe^{III}(dapsox)(H_2O)_2]^+$ and superoxide. Notably, our results also provide indirect experimental support for the inner-sphere mechanism of disproportionation proposed previously in the literature.[47]

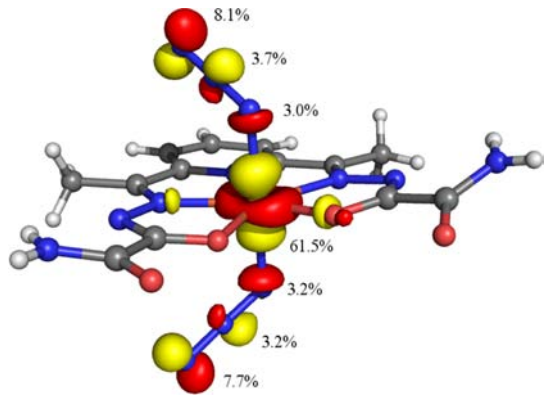

Figure 9. Isosurface plot of the unoccupied Fe 3d_{z^2} based spin-down MO (124b) of $\mathbf{1}_{xtal}$. Contributions from the Fe 3d and azide N 2s and 2p orbitals are indicated.

■ ASSOCIATED CONTENT

Ⓢ Supporting Information

Complete crystallographic details in CIF format; low temperature, frozen solution Abs and MCD data of **1**; 4.5 and 15 K

dx.doi.org/10.1021/ic401098x | Inorg. Chem. 2013, 52, 8909−8918

solid state MCD data of **2**; frozen solution rR spectra of **1** obtained using 514 and 458 nm laser excitation; solid state rR spectrum of **2** obtained with 488 nm laser excitation; and Cartesian coordinates of $\mathbf{1}_{opt}$, $\mathbf{1}_{xtal}$, and $\mathbf{1}_{opt}\cdot\mathbf{H_2O}$. This material is available free of charge via the Internet at http://pubs.acs.org.

AUTHOR INFORMATION

Corresponding Author

*E-mail: brunold@chem.wisc.edu. Phone: (608) 265-9056. Fax: (608) 262-6143.

Present Address

[†]Epic Systems Corporation, 1979 Milky Way, Verona, WI 53593.

Notes

The authors declare no competing financial interest.

ACKNOWLEDGMENTS

T.C.B. thanks the National Institute of Health (GM 64631) for financial support, Dr. Frank Neese (MPI Mülheim) for providing ORCA free of charge, and one of the reviewers for pointing out the existence of an intermolecular hydrogen-bonding interaction in the crystal structure of **2**. This research was supported in part by the National Science Foundation (CHE-0840494).

REFERENCES

(1) Miller, A.-F.; Sorkin, D. L. *Comments Mol. Cell. Biophys.* **1997**, *9*, 1−48.

(2) Fridovich, I. *J. Biol. Chem.* **1997**, *272*, 18515−18517.

(3) Choudhury, S. B.; Lee, J.-W.; Davidson, G.; Yim, Y.-I.; Bose, K.; Sharma, M. L.; Kang, S.- O.; Cabelli, D. E.; Maroney, M. J. *Biochemistry* **1999**, *38*, 3744−3752.

(4) Fridovich, I. *Acc. Chem. Res.* **1972**, *5*, 321−326.

(5) Bull, C.; Niederhoffer, E. C.; Yoshida, T.; Fee, J. A. *J. Am. Chem. Soc.* **1991**, *113*, 4069−4076.

(6) Bull, C.; Fee, J. a. *J. Am. Chem. Soc.* **1985**, *107*, 3295−3304.

(7) McAdam, M. E.; Levelle, F.; Fox, R. A.; Fielden, E. M. *Biochem. J.* **1977**, *165*, 81−87.

(8) Stallings, W. C.; Pattridge, K. A.; Strong, R. K.; Ludwig, M. L. *J. Biol. Chem.* **1984**, *259*, 10695−10699.

(9) Lah, M. S.; Dixon, M. M.; Pattridge, K. A.; Stallings, W. C.; Fee, J. A.; Ludwig, M. L. *Biochemistry* **1995**, *34*, 1646−1660.

(10) Yost, F.; Fridovich, I. *J. Biol. Chem.* **1973**, *248*, 4905.

(11) Schininà, M. E.; Maffey, L.; Barra, D.; Bossa, F.; Puget, K.; Michelson, A. M. *FEBS Lett.* **1987**, *221*, 87−90.

(12) Stallings, W. C.; Metzger, A. L.; Pattridge, K. A.; Fee, J. A.; Ludwig, M. L. *Free Radical Res. Commun.* **1991**, *12*−*3*, 259−268.

(13) Culotta, V. C.; Yang, M.; O'Halloran, T. V. *Biochim. Biophys. Acta* **2006**, *1763*, 747−758.

(14) Raha, S.; Robinson, B. H. *Trends Biochem. Sci.* **2000**, *25*, 502−508.

(15) Simonian, N. A.; Coyle, J. T. *Annu. Rev. Pharmacol. Toxicol.* **1996**, *36*, 83−106.

(16) Valentine, J. S.; Wertz, D. L.; Lyons, T. J.; Liou, L.-L.; Goto, J. J.; Gralla, E. B. *Curr. Opin. Chem. Biol.* **1998**, *2*, 253−262.

(17) Andjelković, K.; Bacchi, A.; Pelizzi, G.; Jeremić, D.; Ivanović-Burmazović, I. *J. Coord. Chem.* **2002**, *55*, 1385−1392.

(18) Liu, G.-F.; Filipović, M.; Heinemann, F. W.; Ivanović-Burmazović, I. *Inorg. Chem.* **2007**, *46*, 8825−8835.

(19) Gutman, C. T.; Brunold, T. C. *Inorg. Chem.* **2012**, *51*, 12729−12737.

(20) Whittaker, M. M.; Whittaker, J. W. *Biochemistry* **1996**, *35*, 6762−6770.

(21) Vance, C. K.; Miller, a. F. *Biochemistry* **1998**, *37*, 5518−5527.

(22) Miller, A.-F.; Sorkin, D. L.; Padmakumar, K. *Biochemistry* **2005**, *44*, 5969−5981.

(23) Tierney, D. L.; Fee, J. A.; Ludwig, M. L.; Penner-Hahn, J. E. *Biochemistry* **1995**, *34*, 1661−1668.

(24) Slykhouse, T. O.; Fee, J. A. *J. Biol. Chem.* **1976**, *251*, 5472−5477.

(25) Misra, H. P.; Fridovich, I. *Arch. Biochem. Biophys.* **1978**, *189*, 317−322.

(26) Jackson, T. A.; Karapetian, A.; Miller, A.-F.; Brunold, T. C. *J. Am. Chem. Soc.* **2004**, *126*, 12477−12491.

(27) Xie, J.; Yikilmaz, E.; Miller, A.-F.; Brunold, T. C. *J. Am. Chem. Soc.* **2002**, *124*, 3769−3774.

(28) Whittaker, J. W.; Whittaker, M. M. *J. Am. Chem. Soc.* **1991**, *113*, 5528−5540.

(29) Grove, L. E.; Xie, J.; Yikilmaz, E.; Karapetyan, A.; Miller, A.-F.; Brunold, T. C. *Inorg. Chem.* **2008**, *47*, 3993−4004.

(30) *APEX2, SADABS, and SAINT Software Reference Manuals*; Bruker-AXS: Madison, WI, 2007−2011.

(31) Neese, F. *ORCA, An Ab Initio, DFT and Semiempirical electronic structure package*, version 2.9.1; 2012.

(32) Becke, A. D. *J. Chem. Phys.* **1993**, *98*, 5648.

(33) Becke, A. D. *J. Chem. Phys.* **1993**, *98*, 1372.

(34) Lee, C.; Yang, W.; Parr, R. G. *Phys. Rev. B* **1988**, *37*, 785.

(35) Schaer, A.; Horn, H.; Ahlrichs, R. *J. Chem. Phys.* **1992**, *97*, 2571.

(36) Weigend, F.; Häser, M. *Theor. Chim. Acta* **1997**, *97*, 331−340.

(37) Schaer, A.; Huber, C.; Ahlrichs, R. *J. Chem. Phys.* **1994**, *100*, 5829.

(38) Hirata, S.; Head-Gordon, M. *Chem. Phys. Lett.* **1999**, *314*, 291−299.

(39) Hirata, S.; Head-Gordon, M. *Chem. Phys. Lett.* **1999**, *302*, 375−382.

(40) *The PyMOL Molecular Graphics System*, L., Version 1.5.0.1; Schrödinger, LLC.

(41) Frisch, M. J.; Trucks, G. W.; Schlegel, H. B.; Scuseria, G. E.; Robb, M. A.; Cheeseman, J. R.; Scalmani, G.; Barone, V.; Mennucci, B.; Petersson, G. A.; Nakatsuji, H.; Caricato, M.; Li, X.; Hratchian, H. P.; Izmaylov, A. F.; Bloino, J.; Zheng, G.; Sonnenberg, J. L.; Hada, M.; Ehara, M.; Toyota, K.; Fukuda, R.; Hasegawa, J.; Ishida, M.; Nakajima, T.; Honda, Y.; Kitao, O.; Nakai, H.; Vreven, T.; Montgomery, Jr., J. A.; Peralta, J. E.; Ogliaro, F.; Bearpark, M.; Heyd, J. J.; Brothers, E.; Kudin, K. N.; Staroverov, V. N.; Kobayashi, R.; Normand, J.; Raghavachari, K.; Rendell, A.; Burant, J. C.; Iyengar, S. S.; Tomasi, J.; Cossi, M.; Rega, N.; Millam, J. M.; Klene, M.; Knox, J. E.; Cross, J. B.; Bakken, V.; Adamo, C.; Jaramillo, J.; Gomperts, R.; Stratmann, R. E.; Yazyev, O.; Austin, A. J.; Cammi, R.; Pomelli, C.; Ochterski, J. W.; Martin, R. L.; Morokuma, K.; Zakrzewski, V. G.; Voth, G. A.; Salvador, P.; Dannenberg, J. J.; Dapprich, S.; Daniels, A. D.; Farkas, Ö.; Foresman, J. B.; Ortiz, J. V.; Cioslowski, J.; Fox, D. J. *Gaussian 09*, Revision C.01; Gaussian Inc.: Wallingford, CT, 2009.

(42) The C/D ratio is defined as $(kT/\beta H)(\Delta\varepsilon/\varepsilon)$ and is equal to $0.9576(\Delta\varepsilon/\varepsilon)$ when H = 7.0 T and T = 4.5 K. This ratio provides a measure of the relative intensity of an electronic transition between the MCD and Abs spectra. Larger ratios are associated with ligand field transitions while smaller ratios are typically observed for charge transfer and $\pi \rightarrow \pi^*$ transitions.

(43) Grove, L. E.; Hallman, J. K.; Emerson, J. P.; Halfen, J. A.; Brunold, T. C. *Inorg. Chem.* **2008**, *47*, 5762−74.

(44) Spiro, T. G.; Czernuszewicz, R. S. In *Physical Methods in Bioinorganic Chemistry*; Que, L., Jr., Ed.; University Science Books: Sausalito, CA, 2000; Chapter Resonance Raman Spectroscopy, pp 59−119.

(45) Li, J.; Noodleman, L.; Case, D. A. In *Inorganic Electronic Structure and Spectroscopy*; Solomon, E. I., Lever, A., Eds.; John Wiley & Sons, Ltd: New York, 1999; Vol. *1*; Chapter Electronic Structure Calculations; Density Functional Methods with Applications to Transition Metal Complexes, p 669.

(46) Sarauli, D.; Meier, R.; Liu, G.-F.; Ivanović-Burmazović, I.; van Eldik, R. *Inorg. Chem.* **2005**, *44*, 7624−7633.

(47) Ivanović-Burmazović, I.; Filipović, M. R. In *Advances in Inorganic Chemistry*; van Eldik, R., Ivanović-Burmazović, I., Eds.; Academic Press: Orlando, FL, 2012; Vol. *64*; Chapter 3, pp 53−95.